Available online at www.sciencedirect.com
SCIENCE DIRECT®
International Journal of Heat and Mass Transfer 47 (2004) 5793–5806
International Journal of HEAT and MASS TRANSFER
www.elsevier.com/locate/ijhmt

Guaranteed fillet weld geometry from heat transfer model and multivariable optimization

A. Kumar, T. DebRoy *

Department of Material Science and Engineering, The Pennsylvania State University, 115 Steidle Building, University Park, PA 16802, United States

Received 30 January 2004

Abstract

Numerical heat transfer models of gas metal arc (GMA) fillet welding do not always predict correct temperature fields and fusion zone geometry. The inaccuracy results, to a large extent, due to the difficulty in correctly specifying several input parameters such as arc efficiency from scientific principles. In order to address this problem, a heat transfer model is combined with an optimization algorithm to determine several uncertain welding parameters from a limited volume of experimental data. The resulting smart model guarantees optimized prediction of weld pool penetration, throat and leg-length within the framework of phenomenological laws. A boundary fitted coordinate system was used to account for the complex fusion zone shape. The weld pool surface profile was calculated by minimizing the total surface energy. Apart from the direct transport of heat from the welding arc, heat transfer from the metal droplets was modeled considering a volumetric heat source. The Levenberg–Marquardt and two versions of conjugate gradient method were used to calculate the optimized values of unknown parameters. An appropriate objective function that represented the difference between the calculated and experimental values of the penetration, throat and leg-length was minimized. The calculated shape and size of the fusion zone, finger penetration characteristic of the GMA welds and the solidified free surface profile were in fair agreement with the experimental results for various welding conditions.

Keywords: Inverse modeling; Parameter estimation; Multivariable optimization; Gas metal arc (GMA) welding; Fillet weld

1. Introduction

In the previous two decades, application of transport phenomena has resulted in improved understanding of fusion welding processes and welded materials [1–4]. Numerical calculations have provided useful information about the thermal cycles and weld pool geometry in both gas metal arc [5–7] and laser welding [8,9]. Computed temperatures have been used to understand the evolution of phase composition [10,11], grain structure [12,13], inclusion structure [14,15], and weld metal composition change owing to both evaporation of alloying elements and dissolution of gases [16,17]. However, these powerful numerical tools have been used mostly

* Corresponding author. Tel.: +1 814 865 1974; fax: +1 814 865 2917.
E-mail address: debroy@psu.edu (T. DebRoy).

0017-9310/$ - see front matter © 2004 Published by Elsevier Ltd.
doi:10.1016/j.ijheatmasstransfer.2004.06.038

Nomenclature

$\mathbf{f}$	matrix representing four unknown parameters in non-dimensional form
$\Delta\mathbf{f}$	matrix representing change in $\mathbf{f}$
$\hat{\mathbf{f}}$	matrix with the values estimated for the parameters
$\mathbf{S}$, $\mathbf{S}^*$	matrices containing sensitivity terms
$\mathbf{V}$	covariance matrix of the estimated parameters
$\mathbf{k}$	unit vector in z-direction
$\mathbf{n}_b$	unit normal vector to the bottom surface
$\mathbf{n}_t$	unit normal vector to the top surface
$\|V_b\|$	norm of the normal vector to the bottom surface
$\|V_t\|$	norm of the normal vector to the top surface
A	constant term in assumed linear efficiency function
B	slope of the variation in assumed linear efficiency function
C_{ij}	correlations coefficients
C_p	specific heat
d	effective height of the volumetric heat source
d_i	direction of descent for the ith variable
e_{RMS}	root-mean-square (RMS) error
f	droplet transfer frequency
f_d	ratio of the radii of droplet volumetric cylindrical heat source and the droplet
f_e	enhancement factor
f_l	liquid fraction
F_b	the heat flux at the bottom surface
F_t	heat flux at the top surface
g	gravitational constant
h	sensible heat
h_v	height of the cylindrical heat source
I	current
J	Jacobian of the transformation
k	thermal conductivity
l	leg-length of the weld pool
L	latent heat of fusion
M	number of available measurements data
N	number of unknown variables
$O(\mathbf{f})$	objective function
p	penetration of the weld pool
P_a	arc pressure
Q_d	total sensible heat input from the metal droplets
r_b	heat distribution parameter
r_d	droplet radius
r_w	wire radius
S_v	power density of a volumetric heat source
t	throat of the weld pool
Δt	interval between two successive drops
T	temperature
T_a	ambient temperature
T_d	droplet temperature
T_l	liquidus temperature
T_s	solidus temperature
U_w	welding speed
v_d	droplet impingement velocity
V	voltage
w_f	wire feeding rate
x, y, z	denotes the physical space
x_v	distance traveled by the center of the slug between the impingement of two successive droplets
z_0	z location of the workpiece top surface

Greek symbols

α	thermal diffusion coefficient
β^k	search step size
γ^k	conjugation coefficient
γ	surface tension of the molten metal
λ	Lagrangian multiplier
λ^k	scalar damping co-efficient
Ω^k	diagonal matrix
ϕ	vertical elevation of top surface with respect to an arbitrarily chosen horizontal plane.
ϕ_s	solidified surface profile
ρ	density of the workpiece material
ρ_w	density of the electrode wire
σ	Stefan–Boltzmann constant
σ_m	standard deviations in the measurements
ξ, η, ζ	computational domain
χ^2_N	value of chi-square distribution with N-degrees of freedom

Superscripts

c	calculated by the numerical heat transfer and fluid flow model
e	experimentally determined values
k	number of iterations

Subscript

m	number of the measurement

for research rather than in the industry [18]. A major difficulty is that some of the input parameters of the model such as the arc efficiency cannot be prescribed based on scientific principles. As a result, the model predictions may not match experimental data because of the uncertainty in the values of some input parameters. In order

to overcome this difficulty, new models are needed that can assure correct prediction of temperature fields and fusion zone geometry.

Fusion welding processes are complex and several component physical processes take place simultaneously during welding. For example, during GMA welding, the work piece receives heat from the arc as well as from the metal droplets formed from the melting of the electrode. The measured values of arc efficiency vary significantly since minor changes in the surface conditions of the workpiece and welding variables affects its value. As a result, the value of the arc efficiency cannot be prescribed with certainty. The transport of the hot metal droplets into the weld pool results in a special shape of the fusion zone often referred as finger penetration [5,19–21]. Previous research has shown that a cylindrical volumetric heat source can adequately represent the time-averaged rate of heat transfer due to impingement of droplets in the spray mode of droplet transfer [5,19,20]. However, the radius of the cylindrical volumetric heat source is specified with trial and error. In complex welding systems, it is customary to take into account the effects of convective heat transport through the use of enhanced thermal conductivity [18,22–25] which is adjusted through trial and error so that the computed temperature profiles agree with experimental data. The value of enhanced conductivity is a property of the specific welding system and not an inherent physical property of the liquid metal. In summary, currently there is no unified basis to accurately prescribe the values of arc efficiency, enhanced thermal conductivity and the diameter of the cylindrical heat source. Although the values of these variables are often assigned from past experience, there is no fundamental scientific basis for assigning these values. If the values of these unknown parameters can be determined from a limited number of experiments, model predictions can be reliable.

The goal of the present work is to develop a model which includes an interactive combination [26–28] of an optimization algorithm, a heat transfer sub-model and a set of experimentally measured weld pool penetration, throat and leg-length. The optimization algorithm minimizes the error between the predicted and the experimentally observed penetration, throat and the leg-length of a fillet weld pool considering the sensitivity of these geometric parameters to each of the unknown welding variables. The complete procedure acts as a smart model that identifies these parameters in an iterative manner starting from a set of their initial guessed values. The input welding parameters and the output weld pool geometry are related by a phenomenological framework of the equations of conservation of mass and energy. Thus, the approach adapted here is inherently different from the neural network technique where the input and output variables are related through a set of hidden nodes and their relationships do not have to comply with any physical law.

2. Direct model

By using a coordinate system attached with the heat source, the following energy conservation equation can be written in the Cartesian coordinate system [5,29]:

$$\nabla \cdot (\alpha \nabla h) - \rho U_{\mathrm{w}} \frac{\partial h}{\partial x} - \rho U_{\mathrm{w}} L \frac{\partial f_{\mathrm{l}}}{\partial x} + S_{\mathrm{v}} = 0 \tag{1}$$

where S_{v} is volumetric heat source whose calculation is discussed in a subsequent section. The sensible heat h is expressed as $h = \int C_P \mathrm{dT}$. The liquid fraction f_{l} is assumed to vary linearly [5,29] with temperature for simplicity

$$f_{\mathrm{l}} = \begin{cases} 1 & T \geqslant T_{\mathrm{l}} \\ \frac{T - T_{\mathrm{s}}}{T_{\mathrm{l}} - T_{\mathrm{s}}} & T_{\mathrm{s}} < T < T_{\mathrm{l}} \\ 0 & T \leqslant T_{\mathrm{s}} \end{cases} \tag{2}$$

Accurate calculation of heat transfer with deformable weld pool surface requires the use of non-orthogonal deformable grid to fit the surface profile. Therefore, the energy conservation equation was transformed from the Cartesian to curvilinear coordinate system. The physical space is denoted by (x, y, z), and the computational domain is represented by (ξ, η, ζ). Fig. 1 shows the transformation from the L-shape physical domain to a simple rectangular computational domain. Only the z-direction in the physical domain is transformed into the ζ direction in the computational domain, while ξ and η directions remain the same as x and y directions, respectively. The transformed energy conservation equation in the curvilinear coordinate system is given [5] as

$$\begin{aligned} &\frac{\partial}{\partial \xi}\left[\alpha\left(\frac{1}{J}\frac{\partial h}{\partial \xi} + q_{13}\frac{\partial h}{\partial \zeta}\right)\right] + \frac{\partial}{\partial \eta}\left[\alpha\left(\frac{1}{J}\frac{\partial h}{\partial \eta} + q_{23}\frac{\partial h}{\partial \zeta}\right)\right] \\ &\quad + \frac{\partial}{\partial \zeta}\left[\alpha\left(q_{31}\frac{\partial h}{\partial \xi} + q_{32}\frac{\partial h}{\partial \eta} + q_{33}\frac{\partial h}{\partial \zeta}\right)\right] \\ &\quad - \rho U_{\mathrm{w}}\left[\frac{\partial}{\partial \xi}\left(\frac{h}{J}\right) + \frac{\partial (q_{13} h)}{\partial \zeta}\right] \\ &\quad - \rho U_{\mathrm{w}} L\left[\frac{\partial}{\partial \xi}\left(\frac{f_{\mathrm{l}}}{J}\right) + \frac{\partial (q_{13} f_{\mathrm{l}})}{\partial \zeta}\right] + \frac{S_{\mathrm{v}}}{J} = 0 \end{aligned} \tag{3}$$

where coefficients q_{13} to q_{33} are defined as

$$\begin{aligned} q_{13} &= q_{31} = -z_\xi = -\frac{\partial z}{\partial \xi} \\ q_{23} &= q_{32} = -z_\eta = -\frac{\partial z}{\partial \eta} \\ q_{33} &= J(z_\xi^2 + z_\eta^2 + 1) = J\left(\left(\frac{\partial z}{\partial \xi}\right)^2 + \left(\frac{\partial z}{\partial \eta}\right)^2 + 1\right) \end{aligned} \tag{4}$$

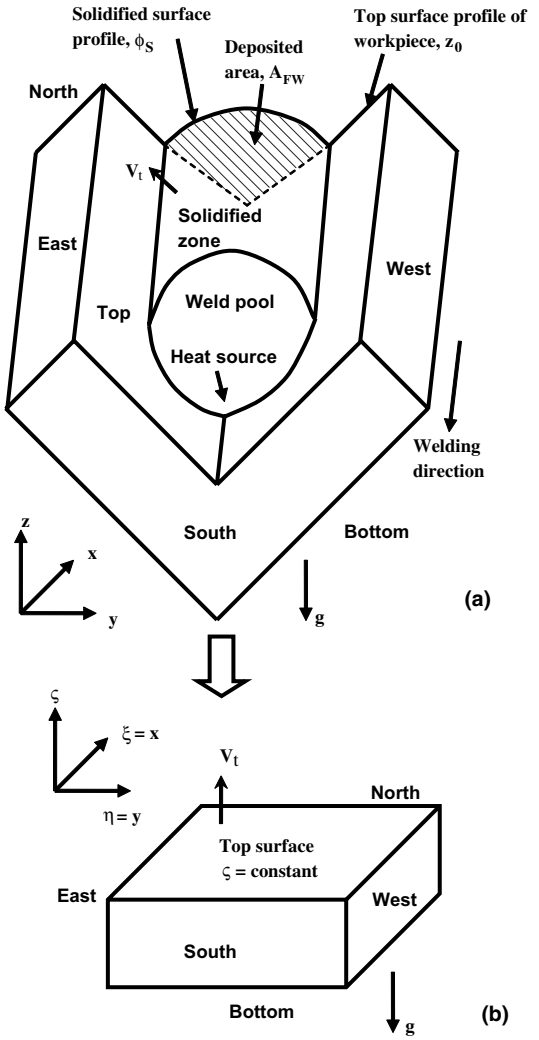

Fig. 1. Schematic plot showing the coordinate transformation from the physical (x, y, z) to the computational domain (ξ, η, ζ) where the transformed energy conservation equation is numerically solved: (a) physical domain, and (b) computational domain. Symbol $\vec{V}_t$ is a normal vector to the top surface. The shadowed area, A_{FW}, is equal to the amount of fed wire per unit length.

The heat flux at the top surface, F_t, is given as [5]

$$\alpha \nabla h \cdot \mathbf{n}_t = F_t = \frac{IV\eta}{2\pi r_b^2} \exp\left(-\frac{x_h^2 + y_h^2}{2r_b^2}\right)(\mathbf{k} \cdot \mathbf{n}_t) - \sigma\varepsilon(T^4 - T_a^4) - h_c(T - T_a) \quad (5)$$

In Eq. (5), the first term on the right hand side is the heat input from the arc defined by a Gaussian heat distribution. The second and third terms represent the heat loss by radiation and convection, respectively. In the curvilinear coordinate, Eq. (5) can be transformed into the following equation [5]:

$$\left.\frac{\partial h}{\partial \zeta}\right|_t = \frac{\frac{F_t \|\mathbf{V}_t\|}{J\alpha} + \frac{\partial h}{\partial \xi} z_\xi + \frac{\partial h}{\partial \eta} z_\eta}{J(z_\xi^2 + z_\eta^2 + 1)} \quad (6)$$

where $\mathbf{V}_t$ is a normal vector to the top surface defined as $\frac{\partial \zeta}{\partial x}\vec{i} + \frac{\partial \zeta}{\partial y}\vec{j} + \frac{\partial \zeta}{\partial z}\vec{k}$ For the bottom surface, the heat flux, F_b, is given as

$$\alpha \nabla h \cdot \mathbf{n}_b = F_b = h_c(T - T_0) \quad (7)$$

Similar to the heat flux equation at the top surface, Eq. (5) is transformed to the following expression in the curvilinear coordinate [5]:

$$\left.\frac{\partial h}{\partial \zeta}\right|_b = \frac{\frac{F_b \|\mathbf{V}_b\|}{J\alpha} + \frac{\partial h}{\partial \xi} z_\xi + \frac{\partial h}{\partial \eta} z_\eta}{J(z_\xi^2 + z_\eta^2 + 1)} \quad (8)$$

The temperatures at other surfaces, i.e., east, west, south, and north surfaces are set to the ambient temperature.

For the calculation of the heat transfer from the metal droplets, the effective height of the volumetric heat source, d, is calculated from the following equation based on energy balance [5,19,20]:

$$d = h_v - x_v + f_d r_d \quad (9)$$

The variables d, h_v, x_v and $f_d r_d$ are shown in Fig. 2. The total sensible heat input from the metal droplets, Q_d, is given as [5]

$$Q_d = \rho_w \pi r_w^2 w_f C_p (T_d - T_l) \quad (10)$$

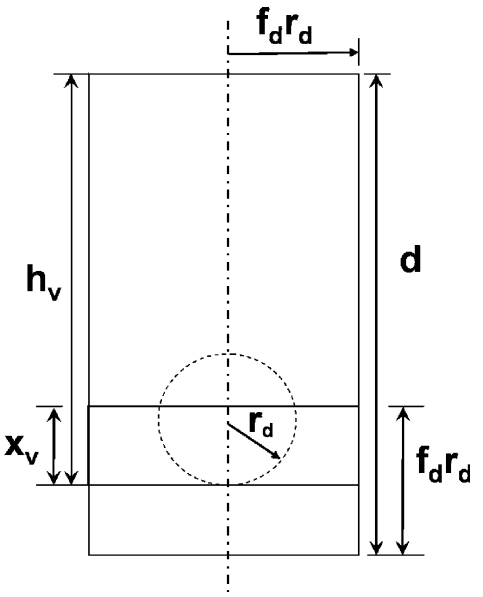

Fig. 2. Schematic diagram of droplet volumetric heat source. All the variables are defined in the nomenclature.

The values of h_v and x_v in Eq. (9) are calculated based on energy balance as [5,19,20]

$$h_v = \left(-\frac{\gamma}{r_d \rho g} + \sqrt{\left[\left(\frac{\gamma}{r_d \rho g} \right)^2 + \frac{r_d v_d^2}{3g} \right]} \right) \tag{11}$$

$$x_v = \left(h_v + \frac{\gamma}{r_d \rho g} \right) \left\{ 1 - \cos \left[\left(\frac{g}{h_v} \right)^{1/2} \Delta t \right] \right\} \tag{12}$$

As shown in Eqs. (11) and (12), calculation of the dimensions of the volumetric heat source requires the knowledge of the droplet transfer frequency, radius and impingement velocity. Rhee [30] and Jones [31] found that the droplet frequency was strongly affected by the welding current under the conditions of this investigation. In this study, the droplet transfer frequency is calculated by fitting their experimental results into a sigmoid function combined with a quadratic function. The resulting equation is given as

$$f = \frac{-243.44}{1 + \exp\left(\dfrac{I - 291.086}{6.06437} \right)} + 323.506 - 0.874 \times I + 0.0025 \times I^2 \quad \text{(Hz)} \tag{13}$$

With the knowledge of the droplet transfer frequency, assuming that the droplets are spherical, the droplet radius, r_d, is given by

$$r_d = \sqrt[3]{\frac{3}{4} r_w^2 w_f \Big/ f} \tag{14}$$

From the computed values of Q_d, r_d and d, the time-averaged power density of the volumetric heat source, S_v, is calculated as follows [5,19]:

$$S_v = \frac{Q_d}{\pi f_d^2 r_d^2 d} \tag{15}$$

It should be noted that Eq. (15) is only valid for grid points within the cylindrical heat source, and the power density is zero outside the cylinder. A brief description of free surface profile calculation is given in Appendix A.

3. Inverse modeling

Inverse model involves the minimization of an objective function that depicts the difference between the computed and measured values [26–28,32–34]. For example, if the penetration, throat and the leg-length of the fusion zone are of interest, an objective function, $O(\mathbf{f})$, can be defined as follows:

$$O(\mathbf{f}) = \sum_{m=1}^{M} (p_m^e - p_m^c)^2 + \sum_{m=1}^{M} (t_m^e - t_m^c)^2 + \sum_{m=1}^{M} (l_m^e - l_m^c)^2 \tag{16}$$

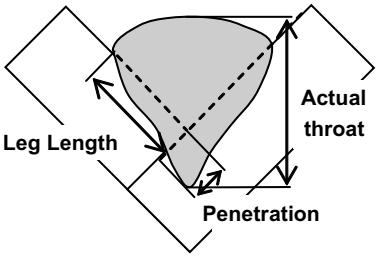

Fig. 3. Nomenclature of the weld geometry in GMA fillet weld.

The penetration, actual throat and leg-length in a GMAW fillet weld are defined in Fig. 3. In the literature, it has been show that arc efficiency varies linearly with the input power [19]. Therefore, in our model also we assumed arc efficiency as linear function of the input power as

$$\eta = A + B \cdot P_i^* \tag{17}$$

$$P_i^* = \frac{IV}{\pi r_w^2 w_f \rho [C_p (T_l - T_a) + L]} \tag{18}$$

Therefore, now we need to find four unknown parameters, A, B, radius of cylindrical volumetric droplet heat source and the enhanced thermal conductivity. In Eq. (16), $\mathbf{f}$ refers to the set of these four unknown parameters in non-dimensional forms i.e. f_1, f_2, f_3 and f_4 such that

$$\{\mathbf{f}\} = \{ f_1 \quad f_2 \quad f_3 \quad f_4 \} = \{ A \quad B \quad f_d \quad f_e \} \tag{19}$$

The enhancement factor, f_e, is defined as the ratio of the enhanced thermal conductivity, k_e, and conductivity of the liquid material, k_L. Evidently, $O(\mathbf{f})$ is a function of $\mathbf{f}$ since $O(\mathbf{f})$ contains variables p_m, t_m and l_m, which are dependent on the parameters included in $\mathbf{f}$. The partial derivatives of weld penetration, actual throat and leg-length with respect to unknown parameters are generally referred as sensitivity coefficients. Assuming that $O(\mathbf{f})$ is continuous and has a minimum value, the optimum values of the four unknowns are obtained by using Levenberg–Marquardt and two different modifications of conjugate gradient method [27] suggested by Fletcher–Reeves [35] and Polak–Ribiere [36].

3.1. Levenberg–Marquardt method

By using Levenburg–Marquardt method, the unknown parameters can be obtained by following equation [18,27,36]:

$$(S + \lambda^k \Omega^k) \cdot \Delta f^k = S^* \tag{20}$$

where λ^k is a scalar damping co-efficient and usually taken as 0.001 and $\mathbf{\Omega}^k$ is the diagonal matrix. The order of $\mathbf{\Omega}^k$ is same as that of the matrix $\mathbf{S}$ and is defined as

$\mathbf{\Omega}^k = \text{diag}\ \mathbf{S}$. The elements of matrix $\mathbf{S}$, and $\mathbf{S}^*$ i.e. S_{ij} and S_i^* can be written as

$$S_{ij} = \sum_{m=1}^{8}\left(\frac{\partial(p_m^c)^k}{\partial f_i}\frac{\partial(p_m^c)^k}{\partial f_j} + \frac{\partial(t_m^c)^k}{\partial f_i}\frac{\partial(t_m^c)^k}{\partial f_j} + \frac{\partial(l_m^c)^k}{\partial f_i}\frac{\partial(l_m^c)^k}{\partial f_j}\right); \quad \text{for } i,j = 1 \text{ to } N \tag{21}$$

$$S_i^* = \sum_{m=1}^{8}\left([p_m^e - (p_m^c)^k]\frac{\partial(p_m^c)^k}{\partial f_i} + [t_m^e - (t_m^c)^k]\frac{\partial(t_m^c)^k}{\partial f_i} + [l_m^e - (l_m^c)^k]\frac{\partial(l_m^c)^k}{\partial f_i}\right); \quad \text{for } i = 1 \text{ to } N \tag{22}$$

where N is the number of unknown variables, i.e. 4. The values of Δf_i^k obtained using Eq. (20) are used to calculate the value of unknown parameters at next iteration by using following relation:

$$f_i^{k+1} = f_i^k + \Delta f_i^k \tag{23}$$

3.2. Conjugate gradient method

The iterative procedure of the Conjugate Gradient method for the minimization of the objective function is given by

$$f_i^{k+1} = f_i^k - \beta^k d_i^k \quad \text{for } i = 1 \text{ to } N \tag{24}$$

The direction of descent for variable i, d_i^k, is a conjugation of the its gradient direction, $\nabla O(f^k)_i$, and its direction of the descent of the previous iteration, d_i^{k-1} and is given as

$$d_i^k = [\nabla O(f^k)]_i + \gamma^k d_i^{k-1} \quad \text{for } i = 1 \text{ to } N \tag{25}$$

where γ^k is the conjugation coefficient. Different expressions are available in the literature for the conjugate coefficient, γ^k. Fletcher and Reeves [35] suggested γ^k as

$$\gamma^k = \frac{\sum_{i=1}^{N}[\nabla O(f^k)]_i^2}{\sum_{i=1}^{N}[\nabla O(f^{k-1})]_i^2} \quad \text{for } k = 1,2,\ldots; \quad \text{and} \quad \gamma^0 = 0 \tag{26}$$

Polak–Ribiere suggested expression for γ^k as [27,36]

$$\gamma^k = \frac{\sum_{i=1}^{N}[\nabla O(f^k)]_i[\nabla O(f_i^k) - \nabla O(f_i^{k-1})]_i}{\sum_{i=1}^{N}[\nabla O(f^{k-1})]_i^2} \quad \text{for } k = 1,2,\ldots; \quad \text{and} \quad \gamma^0 = 0 \tag{27}$$

The search step size, β^k, is obtained as the one which minimizes the objective function. Substituting the values of Taylor series expansion of the unknown parameters at iteration $k+1$ (i.e. Eq. (24) in Eq. (16)), and minimizing with respect to β^k, we get

$$\beta^k = \frac{\sum_{m=1}^{M}\left\{(p_m^c - p_m^e)\left[\sum_{i=1}^{N}\left(\frac{\partial p_m^c}{\partial f_i^k}\right)d_i^k\right] + (t_m^c - t_m^e)\left[\sum_{i=1}^{N}\left(\frac{\partial t_m^c}{\partial f_i^k}\right)d_i^k\right] + (l_m^c - l_m^e)\left[\sum_{i=1}^{N}\left(\frac{\partial l_m^c}{\partial f_i^k}\right)d_i^k\right]\right\}}{\sum_{m=1}^{M}\left[\sum_{i=1}^{N}\left(\frac{\partial p_m^c}{\partial f_i^k}\right)d_i^k + \sum_{i=1}^{N}\left(\frac{\partial t_m^c}{\partial f_i^k}\right)d_i^k + \sum_{i=1}^{N}\left(\frac{\partial l_m^c}{\partial f_i^k}\right)d_i^k\right]^2} \tag{28}$$

The algorithms used for Levenberg–Marquardt and conjugate gradient methods are available in literature [27].

A $72 \times 66 \times 47$ grid system was used and the corresponding solution domain had dimensions of 450 mm in length, 108 mm in width and 18 mm in depth. Spatially non-uniform grids with finer grids near the heat source were used for maximum resolution of variables. The calculations normally converged within 4000 iterations, which took about 6 min for the run of a direct model in a PC with 3.06 GHz Intel P4 CPU and 512 Mb PC2700 DDR-SDRAM.

4. Results and discussion

4.1. Temperature distribution in the weldment

The calculated temperature field for case #1 (Table 1) is shown in Figs. 4 and 5, where the weld pool boundary is represented by the 1745 K solidus isotherm of A-36 steel. The physical properties of the A-36 mild steel workpiece used in the calculations are given in Table 2. Fig. 4 shows that the isotherms in front of the weld pool are compressed while those behind the weld pool are expanded because of the motion of the heat source. This figure also indicates that the depression of the grid lines is maximum under the arc while the grids are elevated in the rear part of the weld pool. Fig. 5 shows the evolution of surface profile during welding. The plane in Fig. 5(a) is located 5 mm ahead of the arc, and this region has not yet melted. The region directly under the arc is shown in Fig. 5(b). This figure also

Table 1
Welding conditions used in the experiments

Case no.	Contact tube to workpiece distance (CTWD) (mm)	Wire feeding rate (mm/s)	Travel speed (mm/s)	Voltage (V)	Estimated current (A)
1	22.2	169.3	4.2	31	312.0
2	22.2	211.7	6.4	31	362.0
3	22.2	169.3	6.4	33	312.0
4	22.2	211.7	4.2	33	362.0
5	28.6	169.3	6.4	31	286.8
6	28.6	169.3	4.2	33	286.8
7	28.6	211.7	4.2	31	331.4
8	28.6	211.7	6.4	33	331.4

Polarity: direct current electrode positive (DCEP).
Joint type: fillet joint, flat position, 90 degree joint angle, and no root gap, as shown in Fig. 1.
Electrode type: 1.32 mm (0.052 in.) diameter solid wire.
Base metal: ASTM A-36 mild steel.
Shielding gas: Ar–10%CO_2.

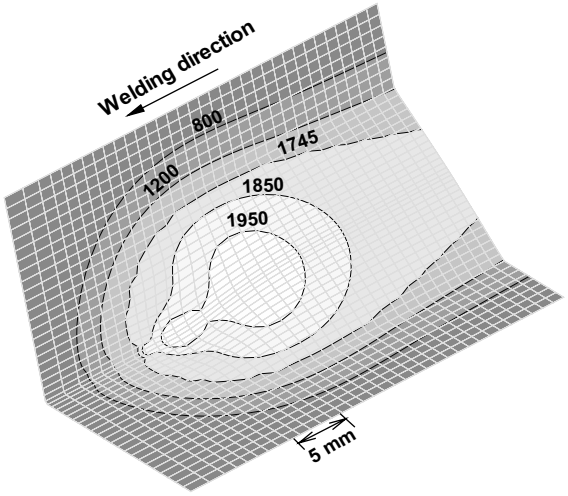

Fig. 4. Calculated temperature field at the weld top surface for case #1 (Table 1). The temperatures are given in Kelvin. The thin solid lines represent the deformable grid system used in the calculation. For clarity, only a portion of the workpiece is shown in this figure.

shows the depression of the free surface due to the arc force. The temperature profiles in Fig. 5(b) clearly show the finger penetration characteristic of the GMA welding. As the monitoring location moves away from the arc, the weld pool surface shows considerably less depression as would be expected from the reduction in arc pressure. Furthermore, the accumulation of the liquid metal in the rear of the weld pool is clearly visible in Fig. 5(c) and (d). The solidified region behind the arc is elevated owing to the filler metal addition. This accumulated metal forms the weld reinforcement after solidification.

4.2. Effect of unknown parameters on the weld pool geometry

The effect of variation of thermal conductivity enhancement factor and arc efficiency on the non-dimensional weld geometry i.e. leg-length, throat and penetration are shown in Fig. 6(a)–(c). The non-dimensional values of the leg-length, throat and penetration shown in Fig. 6(a)–(c) are obtained by dividing the numerically computed value with the corresponding experimentally obtained value. The increase in enhancement factor (f_e) leads to higher heat conduction inside the workpiece which tends to minimize the temperature gradient. Since most of the heat flows in the downward direction, the value of leg-length does not vary much with increase in f_e for a fixed value of arc efficiency as shown in Fig. 6(a). However, when the arc efficiency is increased, from 0.40 to 0.80, a 30% increase in the non-dimensional leg-length is achieved because the leg-length depends mainly on the heat input from the arc.

In contrast to leg-length, penetration is dictated by heat transfer due to impinging metal droplets. The sensible heat of droplets is distributed mainly to a region directly under the arc and the penetration is affected by the distribution of heat. The enhanced thermal conductivity improves heat transfer rate. The more efficient distribution of a given amount of heat from the droplets in all directions leads to smaller penetration as shown in Fig. 6(b). This figure also shows that the penetration increases with higher heat input. Fig. 6(c) shows that the computed non-dimensional throat does not vary significantly with either arc efficiency or the enhancement factor for given wire feed rate and welding speed. This behavior is expected since the dimensions of the throat depend largely on the rate of mass addition. The trends shown in Fig. 6(a)–(c) were true for other values of

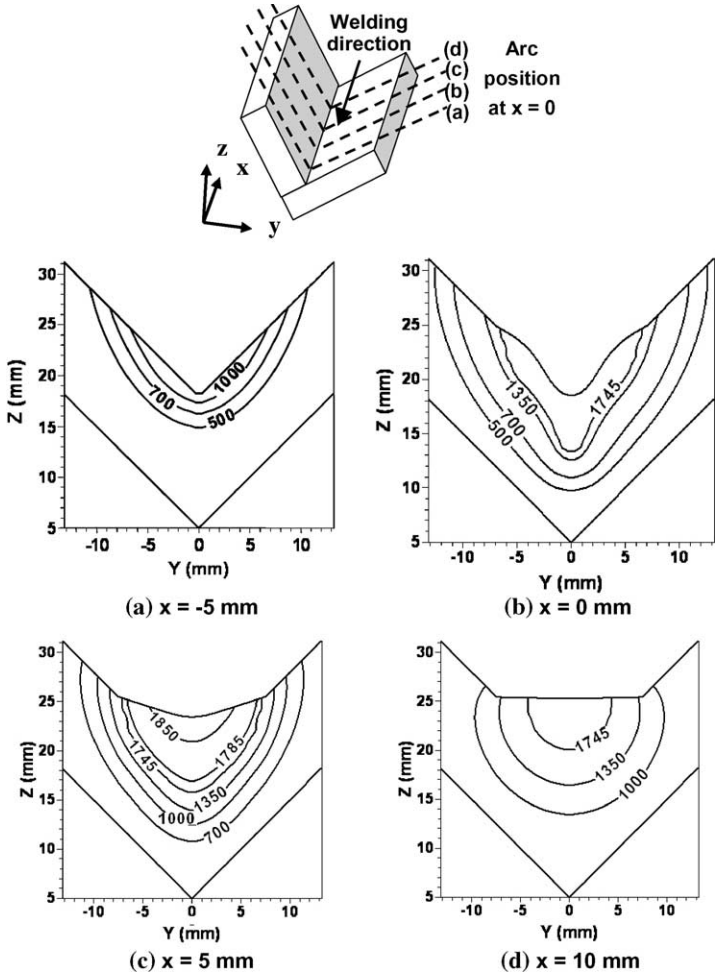

Fig. 5. Calculated temperature field at different cross sections planes perpendicular to the welding direction for case#1 (Table 1): (a) 5 mm ahead of the arc location; (b) directly under the arc; (c) 5 mm rear of the arc location; (d) 10 mm rear of the arc location. The temperatures are given in Kelvin.

Table 2
Physical properties of the mild steel workpiece used in the calculation

Physical property	Value
Liquidus temperature, T_L (K)	1785.0
Solidus temperature, T_S (K)	1745.0
Density of metal, ρ (kg/m^3)	7200
Thermal conductivity of solid, k_S, (J/m s K)	21.0
Specific heat of solid, C_{PS} (J/kg K)	703.4
Specific heat of liquid, C_{PL} (J/kg K)	808.1
Surface tension of liquid metal (N/m)	1.2

current, voltage, wire feed rate, CTWD and welding speed investigated.

Fig. 6(a) shows that there are several combinations of η and f_e that can provide acceptable values of leg-length. Similarly, from Fig. 6(b) and (c), we can obtain independent combinations of η and f_e that would result in good agreement between the computed and the experimental values of penetration and throat. However, there is no guarantee that the same combination of η and f_e would lead to satisfactory prediction of all weld dimensions given by $p_m^* = t_m^* = l_m^* = 1$. Efficiency also varies almost linearly with the heat input [19] which increases the complexity of the problem. With the increase in the welding current, the drops become progressively smaller and their rate of transfer increases because of higher electromagnetic force acting on the droplets [19]. In short, heat transfer in the GMAW process is highly complex because of the interaction of several simultaneously occurring physical processes. Of the many variables that define a particular weld, three parameters, i.e., arc efficiency, enhanced thermal conductiv-

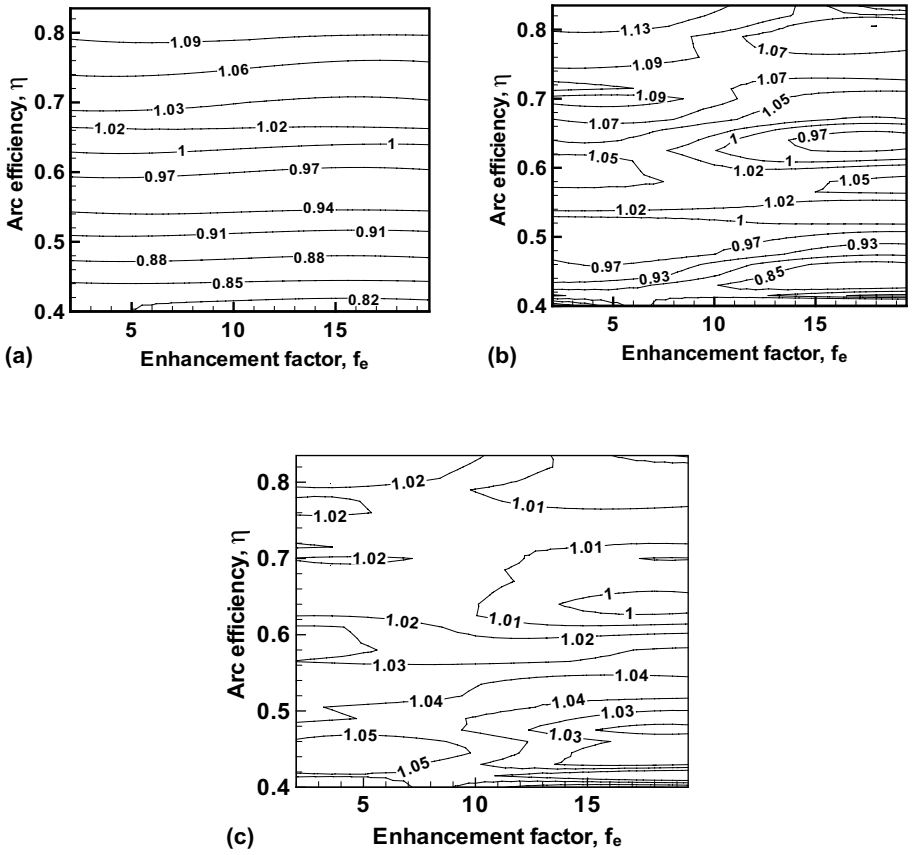

Fig. 6. Contour plot of non-dimensional: (a) leg-length; (b) penetration; (c) actual throat calculation, for $I = 312$ A, $V = 31.0$ V, welding speed = 0.42 cm/s, wire feed = 16.93 cm/s, CTWD = 2.22 cm and $f_d = 2.0$.

ity and radius of volumetric cylindrical heat source, cannot be defined with certainty from fundamental principles of science. Therefore, determination of these parameters from a limited volume of experimental data is important.

4.3. Estimation of unknown parameters

To calculate the optimized values of arc efficiency, enhanced thermal conductivity and radius of volumetric cylindrical heat source, a set of initial guessed values are necessary for these parameters. Table 3 compares the results obtained by using three methods of optimization for the initial guessed values of $A = 0.65$, $B = 0.05$, $f_d = 2.0$, $f_e = 25.0$ that define the uncertain parameter values. Polak and Ribiere's CG method gives better convergence of the objective function than the other two methods. The minimum value of the objective function, 0.39, is achieved after 14 iterations by this method. LM and Fletcher–Reeves's CG method produced values of 0.42 and 0.40 in 14 and 27 iterations, respectively. As shown in Fig. 7, the objective function did not decrease continuously with iterations. After reaching low values, the objective function started to oscillate with iterations.

The optimized combination of A, B, f_d and f_e obtained from all the three optimization methods presented in Table 3 shows a higher range of arc efficiency for all the experimental cases presented in Table 1. These values are higher than the reported values of arc efficiency [19] for the GMAW process. Therefore, these values do not seem to lie within the expected range of values. Again, Fig. 8 shows that Polak and Ribiere's CG method give better convergence of the objective function compared to other two optimization methods. The minimum value of $O(\mathbf{f})$ achieved is 0.35 within 18 iterations by this method. On the other hand, LM and Polak–Ribiere's CG method produced a value of 0.44 and 0.38 in 17 and 16 iterations, respectively. After reaching the low values, again objective function starts oscillating and do not decrease beyond these values. This oscillation in objective function is because the inverse problems become ill-conditioned near the optimal solution [26–28].

Based on the results obtained for two sets of input values of unknown parameters in Tables 3 and 4, we

Table 3
Comparison of results obtained by using LM method and the two versions of CG method for the initial guessed values of $A = 0.65$, $B = 0.05$, $f_d = 2.0$ and $f_e = 25$

Method	Parameter	Estimates	$O(\mathbf{f})$	Iterations	Obtained range of arc efficiency by using values of A and B
LM method	A	0.64	0.42	14	0.81–0.86
	B	0.07			
	f_d	1.48			
	f_e	26.20			
CG method—Polak and Ribiere	A	0.50	0.39	14	0.82–0.90
	B	0.13			
	f_d	1.97			
	f_e	24.01			
CG method—Fletcher and Reeves	A	0.56	0.40	27	0.83–0.90
	B	0.11			
	f_d	2.03			
	f_e	24.02			

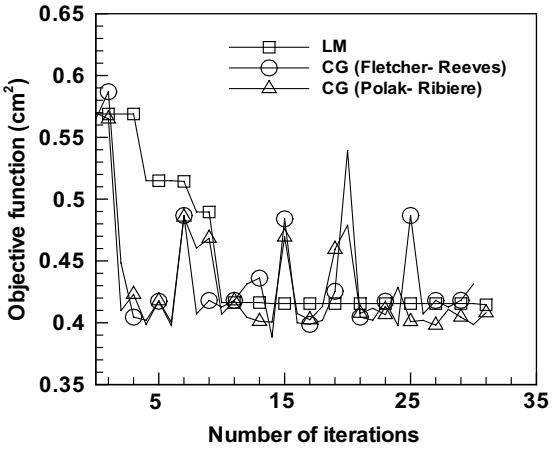

Fig. 7. Comparison of calculation progress for all the four unknowns and the objective function using LM method and the two versions of CG method for the initial guessed values of $A = 0.65$, $B = 0.05$, $f_d = 2.0$, $f_e = 25.0$.

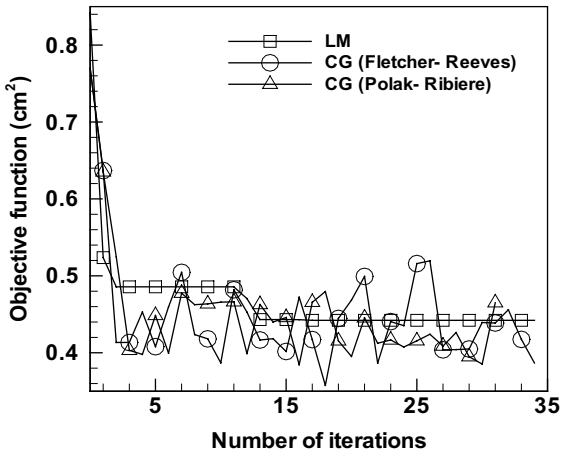

Fig. 8. Comparison of calculation progress for all the four unknowns and the objective function using LM method and the two versions of CG method for the initial guessed values of $A = 0.3$, $B = 0.15$, $f_d = 2.5$, $f_e = 10.0$.

can see that $O(\mathbf{f})$ does not vary much after it attains a value of about 0.40. It is certainly inappropriate to relate these optimum values as an universal feature of GMAW process. A rational way to describe the optimum combination of the four unknown parameters is as a set of system properties that is inherent within the eight measured weld samples that have governed the optimization calculation. Based on the minimum value of the objective function, $O(\mathbf{f})$, we can propose the final values of the unknown parameters as

$$\eta = 0.419 + 5.61 \times 10^{-6}\ IV/w_f \tag{29}$$

$$f_d = 2.67 \tag{30}$$

$$f_e = 12.00 \tag{31}$$

where I is current in Amp, V is voltage in volts and w_f is wire feed rate in m/s. Eq. (29) shows that the arc efficiency increases with increase in input power and decrease in wire feed rate. The values of arc efficiency also lies in the range of 66–85% as reported in the literature [19,24]. Arc efficiency decreases with wire feed rate because more power is necessary for melting wire at high wire feed rate. As a result, less power is available to the workpiece. The optimized value of enhancement factor for thermal conductivity is found to be 12.0. Hong et al. [22,24] suggested an enhancement factor of 12 to 20 for GMAW with 150 A and 25 V. Choo and Szekely [25] suggested an enhancement factor of more than 8 for a current of 100 A. Although the values available in the literature [24,25] are for specific welding condi-

Table 4
Comparison of results obtained by using LM method and the two versions of CG method for the initial guessed values of $A = 0.3$, $B = 0.15$, $f_d = 2.5$ and $f_e = 10$

Method	Parameter	Estimates	$O(\mathbf{f})$	Iterations	Obtained range of arc efficiency by using values of A and B
LM method	A	0.36	0.44	17	0.71–0.79
	B	0.14			
	f_d	1.56			
	f_e	8.4			
CG method—Polak and Ribiere	A	0.42	0.35	18	0.69–0.76
	B	0.11			
	f_d	2.67			
	f_e	12.00			
CG method—Fletcher and Reeves	A	0.47	0.38	16	0.67–0.72
	B	0.08			
	f_d	2.46			
	f_e	12.01			

tions, they show that the optimized values obtained in this work are somewhat similar to those reported in the literature.

4.4. Confidence region analysis

We assumed that the errors in the experimental data were random, i.e., the kind that will cancel each other if we take enough data. However, measurements having systematic errors do not cancel each other with averaging. So, the minimum value of the objective function is subject to systematic errors, thermal stress induced distortion in the weld samples and the assumptions used in the heat transfer model. Considering that all the measurements have the same error, an RMS error can be defined as [27]:

$$e_{\mathrm{RMS}} = \sqrt{\frac{1}{M} O(\mathbf{f})} \tag{32}$$

For minimum value of objective function obtained using Polak and Ribiere's CG method, we get $e_{\mathrm{RMS}} = 0.21$ cm. Assuming, 25% of this e_{RMS} value is due to systematic errors in experimental measurements, the standard deviation (σ_m) in the experimental measurements can be assumed equal to 0.05 cm. By performing a statistical analysis it is possible to assess the accuracy of the calculated values. If the errors are Gaussian in distribution, the minimization of the chi-square norm can be used for testing the accuracy of the parameters. The reduced covariance matrix, $\mathbf{V}$, of the estimated parameters is given by [32,33,37]

$$V = \begin{bmatrix} \mathrm{cov}(f_1,f_1) & \mathrm{cov}(f_1,f_2) & \mathrm{cov}(f_1,f_3) & \mathrm{cov}(f_1,f_4) \\ \mathrm{cov}(f_2,f_1) & \mathrm{cov}(f_2,f_2) & \mathrm{cov}(f_2,f_3) & \mathrm{cov}(f_2,f_4) \\ \mathrm{cov}(f_3,f_1) & \mathrm{cov}(f_3,f_2) & \mathrm{cov}(f_3,f_3) & \mathrm{cov}(f_3,f_4) \\ \mathrm{cov}(f_4,f_1) & \mathrm{cov}(f_4,f_2) & \mathrm{cov}(f_4,f_3) & \mathrm{cov}(f_4,f_4) \end{bmatrix} = \mathbf{S}^{-1}\sigma_m^2 \tag{33}$$

The standard deviations for the estimated parameters can be obtained from the diagonal elements of $\mathbf{V}$ as

$$\sigma_{f_j} \equiv \sqrt{\mathrm{cov}(f_j,f_j)} = \sqrt{V_{jj}} \quad \text{for } j = 1,\ldots,N \tag{34}$$

where V_{jj} is the jth element in jth row of the matrix $\mathbf{V}$. Confidence intervals at the 95% confidence levels for the estimated parameters are obtained as

$$f_j - 1.96\sigma_{f_j} \leqslant f_j \leqslant f_j + 1.96\sigma_{f_j} \quad \text{for } j = 1,\ldots,N \tag{35}$$

The confidence intervals calculated by using Eqs. (34) and (35) for obtained optimized values are listed in Table 5. But, confidence intervals for individual parameters do

Table 5
Obtained confidence range and joint confidence region of optimized values of unknown parameters for a standard deviation of 0.05 cm in the measurements

Parameter	Optimized estimates	Standard deviation	Confidence range	Joint confidence region
A	0.43	0.01	$0.41 \leqslant A \leqslant 0.45$	$(55.27A^2 + 2.10B^2 + 1.36f_d^2 + 0.15f_e^2 + 19.9AB - 8.38Af_d - 3.21Af_e$
B	0.12	0.01	$0.10 \leqslant B \leqslant 0.14$	$-0.16Bf_d + 0.06Bf_e + 0.01f_df_e - 76.90A - 17.21B - 0.71f_d$
f_d	2.70	0.02	$2.66 \leqslant f_d \leqslant 2.74$	$-3.47f_e + 47.27) \leqslant 0$
f_e	12.20	0.15	$11.90 \leqslant f_e \leqslant 12.50$	

not provide a good approximation for a joint confidence region for the estimated parameters taken as a set. The joint confidence region for the estimated parameters [32,33,37] is given by:

$$(\hat{f}-f)^{\mathrm{T}}V^{-1}(\hat{f}-f)\leqslant\chi_N^2 \tag{36}$$

The calculated joint confidence interval for obtained optimized values is listed in Table 5. It is clear from the values listed in Table 5 that these confidence intervals can be used to select our optimized values of unknown parameters. Table 5 shows that the optimized values of the unknown parameters fall inside joint confidence region.

Fig. 9 shows the calculated values of p_m^*, l_m^* and t_m^* using the optimized values of the unknown parameters. The results show that the optimized values of the unknown parameters do result in correct predictions of the fusion zone geometry. The calculated bead shape using the optimized value of the efficiency, volumetric cylindrical heat source radius and enhanced thermal conductivity, for cases # 2 and # 6 in Table 1 are shown in Fig. 10. The calculated fusion zone geometry for both the cases agrees reasonably well with the corresponding experimental results. Some discrepancy between the experimental surface profile and the computed results is due to thermal stress induced distortion as can be evidenced from the gap between the two plates. On the whole, the geometric features of the fillet weld could be satisfactorily predicted by the using the optimized values of unknown parameters in the numerical heat transfer model.

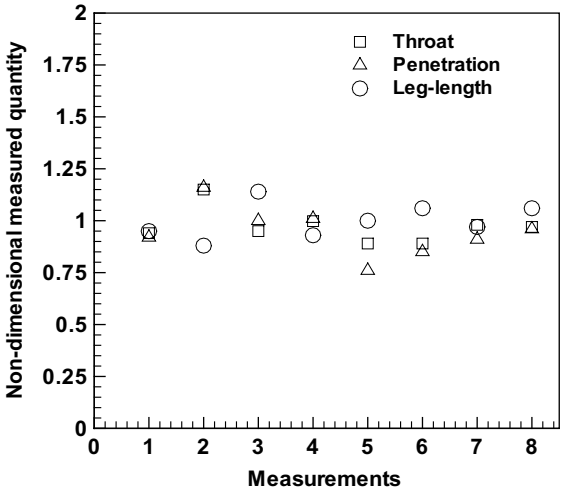

Fig. 9. Computed values of non-dimensional throat, penetration and leg-length using the optimized set of all the four unknown parameters for all the eight measurement cases listed in Table 1.

5. Conclusions

The coupled influence of arc efficiency, enhanced thermal conductivity and the radius of the volumetric cylinderical heat source on heat transfer during GMA welding is complex. The values of these unknown parameters can be determined from a limited volume of experimental data using an appropriate optimization model and a heat transfer model for GMA fillet welding. Based on this approach, a smart phenomenological model for GMA fillet welding involving numerical calculation of heat transfer and parameter optimization was developed. The model solved energy conservation equations in a curvilinear coordinate to obtain the temperature fields and surface profile during GMA fillet welding. Levenberg–Marquardt method, Fletcher–Reeve and Polak–Ribiere's modified conjugate gradient methods were considered for multivariable optimization. A relation between arc efficiency and input power and wire feed rate is proposed. The optimized values of arc efficiency, radius of volumetric heat source and enhanced thermal conductivity were found to be within

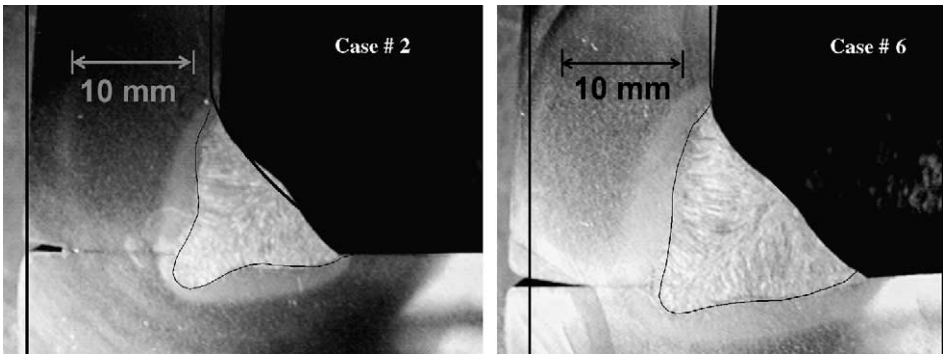

Fig. 10. Comparison between the calculated and experimental weld geometry for cases # 2 and # 6 given in Table 1. The contour line represents the calculated weld pool geometry.

the range of values reported in the literature. Using the values of unknown parameters determined by this model, the calculated shape and size of the fusion zone, finger penetration characteristic of the GMA welds and the solidified free surface profile were calculated for several welding conditions. Good agreement between the model predictions and the experimental data of leg length, the penetration depth and the actual throat for various welding conditions show that this approach is promising.

Appendix A

The weld pool free surface profile is determined by minimizing the total surface energy, which includes surface tension energy, the potential energy owing to gravity and the work performed by the arc force displacing the weld pool surface. The governing equation for the free surface profile is given by [5]

$$\gamma\left\{\frac{(1+\phi_y^2)\phi_{xx}-2\phi_x\phi_y\phi_{xy}+(1+\phi_x^2)\phi_{yy}}{(1+\phi_x^2+\phi_y^2)^{3/2}}\right\} = \rho g\phi + P_a + \lambda \quad (A.1)$$

The arc pressure, P_a, is expressed as [5]:

$$P_a = \frac{F}{2\pi\sigma_p^2}\exp\left(-\frac{x^2+y^2}{2\sigma_p^2}\right) \quad (A.2)$$

where

$$F = -0.04017 + 0.0002553 \times I \quad (\mathrm{N}) \quad (A.3)$$

$$\sigma_p = 1.4875 + 0.00123 \times I \quad (\mathrm{mm}) \quad (A.4)$$

The boundary conditions for the free surface equation are given as

$$\text{At the front pool boundary: } \phi = z_0 \quad (A.5a)$$

$$\text{At the rear pool boundary: } \frac{\partial\phi}{\partial x} = 0 \quad (A.5b)$$

Here the front and rear pool boundaries are defined so that the temperature gradient along the x direction ($\mathrm{d}T/\mathrm{d}x$) is positive at the front pool boundary and negative at the rear boundary. As shown in Fig. 1(a), the deposited area, A_{FW}, at a solidified cross section of the fillet weld is equal to the amount of fed wire per unit length:

$$\int(\phi_s - z_0)\,\mathrm{d}y - \frac{\pi r_w^2 w_f}{U_w} = 0 \quad (A.6)$$

Calculation of the free surface profile requires simultaneous solution of both the free surface Eq. (A.1) and the constraint Eq. (A.6). Eq. (A.1) is discretized using the finite difference method and then solved using the Gauss–Seidel point-by-point method for an assumed λ. The resulting free surface profile is applied to the constraint Eq. (A.6) and the residual (defined as the left-hand side of Eq. (A.6)) is evaluated. The value of λ is determined iteratively until both Eqs. (A.1) and (A.6) are satisfied.

References

[1] S.A. David, T. DebRoy, Current issues and problems in welding science, Science. 257 (1997) 497–502.
[2] T. DebRoy, S.A. David, Physical processes in fusion welding, Rev. Mod. Phys. 67 (1995) 85–112.
[3] H. Zhao, D.R. White, T. DebRoy, Current issues and problems in laser welding of automotive aluminum alloys, Int. Mater. Rev. 44 (1999) 238–266.
[4] T. DebRoy, Computational modeling: a path to expand the knowledge base in fusion welding, Indian Weld. J. 36 (2003) 59–66.
[5] C.-H. Kim, W. Zhang, T. DebRoy, Modeling of temperature field and solidified surface profile during gas metal arc fillet welding, J. Appl. Phys. 94 (2003) 2667–2679.
[6] W. Zhang, G. Roy, J.W. Elmer, T. DebRoy, Modeling of heat transfer and fluid flow during gas tungsten arc spot welding of low carbon steel, J. Appl. Phys. 93 (2003) 3022–3033.
[7] A. Kumar, T. DebRoy, Calculation of three-dimensional electromagnetic force field during arc welding, J. Appl. Phys. 94 (2003) 1267–1277.
[8] H. Zhao, T. DebRoy, Macro-porosity free aluminum alloy weldments through numerical simulation of keyhole mode laser welding, J. Appl. Phys. 93 (2003) 10089–10096.
[9] X. He, P.W. Fuerschbach, T. DebRoy, Heat transfer and fluid flow during laser spot welding of 304 stainless steel, J. Phys. D: Appl. Phys. 36 (2003) 1388–1398.
[10] J.W. Elmer, T.A. Palmer, W. Zhang, B. Wood, T. DebRoy, Kinetic modeling of phase transformations occurring in the HAZ of C–Mn steel welds based on direct observations, Acta Mater. 51 (2003) 3333–3349.
[11] W. Zhang, J.W. Elmer, T. DebRoy, Modeling and real time mapping of phases during GTA welding of 1005 Steel, Mater. Sci. Eng. A 333 (2002) 321–335.
[12] S. Mishra, T. DebRoy, Grain growth in the heat-affected zone of Ti–6Al–4V welds: measurements and three dimensional Monte Carlo simulation, in: S.A. David, T. DebRoy, J.C. Lippold, H. Smartt, J.M. Vitek (Eds.), Proceedings of Trends in Welding Research, ASM International, Materials Park, OH, 2003, pp. 197–202.
[13] S. Sista, T. DebRoy, Three dimensional Monte Carlo simulation of grain growth in zone refined iron, Metall. Mater. Trans. B 32 (2001) 1195–1201.
[14] T. Hong, T. DebRoy, Non-isothermal growth and dissolution of inclusions in liquid steels, Metall. Mater. Trans. B 34 (2003) 267–269.
[15] T. Hong, T. DebRoy, Effects of time, temperature and steel composition on the growth and dissolution of inclusions in liquid steels, Ironmaking Steelmaking 28 (2001) 450–454.
[16] S.A. David, R. Trivedi, M.E. Eshelman, J.M. Vitek, S.S. Babu, T. Hong, T. DebRoy, Observation of weld pool solidification using transparent metal-analog systems, J. Appl. Phys. 93 (2003) 4885–4895.

[17] H. Zhao, T. DebRoy, Weld metal composition change during conduction mode laser welding of 5182 aluminum alloy, Metall. Mater. Trans. B 32 (2001) 163–172.
[18] A. De, T. DebRoy, Probing unknown welding parameters from convective heat transfer calculation and multivariable optimization, J. Phys. D: Appl. Phys. 37 (2004) 140–150.
[19] J.F. Lancaster, The Physics of the Welding, second ed., Pergamon, Oxford, 1986.
[20] S. Kumar, S.C. Bhaduri, Three-dimensional finite element modeling of gas metal arc welding, Metall. Trans. B 25 (1994) 435–441.
[21] S.-H. Cho, J.-W. Kim, Thermal analysis of horizontal fillet joints by considering bead shape in gas metal arc welding, Sci. Technol. Weld. Join. 6 (2001) 220–224.
[22] K. Hong, D.C. Weckmann, A.B. Strong, W. Zheng, Modelling turbulent thermofluid flow in stationary gas tungsten arc weld pools, Sci. Technol. Weld. Join. 7 (2002) 125–136.
[23] P.G. Jonsson, J. Szekely, R.T.C. Choo, T.P. Quinn, Mathematical models of transport phenomena associated with arc welding process: a survey, Model. Simul. Mater. Sci. Eng. 2 (1994) 995–1016.
[24] K. Hong, D.C. Weckman, A.B. Strong, E. Pardo, Prediction of gas metal arc weld bead geometry using a three-dimensional finite element thermal model, in: S.I. Guceri (Ed.), Proceedings of the First International Conference on Transport Phenomena in Processing, Technomic Publishers, 1992, pp. 626–635.
[25] R.T.C. Choo, J. Szekely, The possible role of turbulence in GTA weld pool behaviour, Weld. J. 73 (1994) 25–31.
[26] J.V. Beck, B. Blackwell, C.R. St. Clair, Inverse Heat Conduction: Ill-posed Problems, Wiley International, New York, 1985.
[27] M.N. Ozisik, H.R.B. Orlande, Inverse Heat Transfer: Fundamentals and Applications, first ed., Taylor and Francis, New York, 2000.
[28] O.M. Alifanov, Inverse Heat Transfer Problems, Springer-Verlag, New York, 1994.
[29] K. Mundra, T. DebRoy, K.M. Kelkar, Numerical prediction of fluid flow and heat transfer in welding with a moving heat source, Numer. Heat Transfer A 29 (1996) 115–129.
[30] S. Rhee, E. Kannatey-Asibu Jr., Observation of metal transfer during gas metal arc welding, Weld. J. 71 (1992) 381–386.
[31] L.A. Jones, T.W. Eagar, J.H. Lang, A dynamic model of drops detaching from a gas metal arc welding electrode, J. Phys. D: Appl. Phys. 31 (1998) 107–123.
[32] J.V. Beck, K.J. Arnold, Parameter Estimation in Engineering and Science, first ed., John Wiley and Sons, New York, 1977.
[33] Y. Bard, Nonlinear Parameter Estimation, first ed., Academic Press, New York, 1974.
[34] J. Dennis, R. Schnabel, Numerical methods for unconstrained optimization and non-linear equations, Prentice-Hall, Englewood Cliffs, NJ, 1983.
[35] R. Fletcher, C.M. Reeves, Function minimization by conjugate gradients, Comp. J. 7 (1964) 149–154.
[36] J. Nocedal, S.J. Wright, Numerical Optimization, first ed., Springer-Verlag, New York, 1999.
[37] G.P. Box, W.G. Hunter, J.H. Hunter, Statistics for Experimenters, first ed., John Wiley & Sons, New York, 1978.